

# Impacts of Hurricane Irma (2017) on ocean transport processes

Thomas Dobbelaere<sup>a,\*</sup>, Milan Curcic<sup>b</sup>, Matthieu le Hénaff<sup>c,d</sup>, Emmanuel Hanert<sup>a,e</sup>

<sup>a</sup>*Eath and Life Institute (ELI), UCLouvain, Louvain-la-Neuve, Belgium*

<sup>b</sup>*Rosenstiel School of Marine and Atmospheric Sciences (RSMAS), University of Miami, Coral Gables, Florida, USA*

<sup>c</sup>*Cooperative Institute for Marine and Atmospheric Studies (CIMAS), University of Miami, Miami, Florida, USA*

<sup>d</sup>*Atlantic Oceanographic and Meteorological Laboratory (AOML), NOAA, Miami, Florida, USA*

<sup>e</sup>*Institute of Mechanics, Materials and Civil Engineering (IMMC), UCLouvain, Louvain-la-Neuve, Belgium*

---

## Abstract

Tropical cyclones are becoming more intense and more frequent. Their effect is particularly acute in coastal areas where they cause extensive damage leading to an influx of debris, sediments and waste to the sea. However, most coastal ocean models do not represent heavy-wind transport processes correctly as they do not couple the hydrodynamics with the wind-generated waves. This may lead to significant errors in simulations of tropical cyclones. Here, we investigate current-wave interactions during a major hurricane and assess their impact on transport processes. We do that by coupling the unstructured-mesh coastal ocean model SLIM with the spectral wave model SWAN, and applying it to the Florida Reef Tract during Hurricane Irma (September 17). We show that the coupled model successfully reproduces the wave behavior, the storm surge and the ocean currents during the passage of the hurricane. We then use the coupled and uncoupled wave-current model to simulate the transport

---

\*Corresponding author

Email address: [thomas.dobbelaere@uclouvain.be](mailto:thomas.dobbelaere@uclouvain.be) (Thomas Dobbelaere)

of passive drifters. We show that the wave radiation stress gradient alone can lead to changes of up to 1 m/s in the modeled currents, which in turn leads to differences of up to 5 km in the position of drifting material over the duration of the hurricane. The Stokes drift however appears to be up to 4 times more intense and should thus be considered in priority. Wave-current interactions therefore strongly impact the transport of drifting material such as sediments and debris in the aftermath of a hurricane. They should thus be taken into account in order to correctly assess its overall impact.

*Keywords:* Hurricane, Ocean transport, Wave-current interactions

---

## **1. Introduction**

Tropical cyclones are becoming more intense and more frequent (Bhatia et al., 2019; Kossin et al., 2020). This increase is likely due to climate change and will probably continue in the future (Knutson et al., 2020). However, estimating the impact of tropical cyclones on the coastal ocean circulation remains a challenge. Understanding wave-current interactions and representing their impact on coastal ocean transport processes is central to many coastal activities such as dredging, erosion management, Oil & Gas, search and rescue, and insurance (Bever and MacWilliams, 2013; Li and Johns, 1998; Breivik et al., 2013). All these activities require wave-current models to predict the impact of tropical cyclones on the coastal circulation and on water-level changes.

Wave-current interactions during a cyclone are highly nonlinear and vary significantly in space and time (Wu et al., 2011). Wave-induced currents are generated by wave radiation stress gradients (Longuet-Higgins, 1970), affecting water levels near shorelines and wave breaking points (Longuet-Higgins and Stewart, 1964). Changes in water levels and currents, in turn, affect the motion and evolution of the waves (Sikirić et al., 2013). Coupled wave-current models hence require the calculation of the full directional wave spectrum in order to correctly reproduce the dynamics of wind-driven surface

waves. This is usually achieved by spectral wave models, which describe the evolution of the wave energy spectrum. As of today, the most popular spectral wave models are WAM (WAMDI Group, 1988), SWAN (Booij et al., 1999), and WAVEWATCH III (Tolman et al., 2009). Among these models, SWAN is more fitted to coastal applications, as it represents depth-induced wave breaking and triad wave-wave interactions, while implementing numerical techniques adapted to small-scale, shallow water regions (Booij et al., 1999).

Coastal oceans are characterized by the complex topography of the coastline and the presence of islands, reefs and artificial structures. Traditional structured-grid models lack the flexibility to simulate near-shore processes at a sufficiently small scale. Instead, unstructured-mesh models easily adapt to the topography and are hence better suited to coastal processes (Fringer et al., 2019). Capturing the impact of the topography on wave interactions becomes even more important in the case of tropical cyclones. Heavy winds generate large wind-waves and disturb ocean conditions (Liu et al., 2020) by causing coastal upwellings on continental shelves (Smith, 1982) and inducing strong currents, waves and storm surges in nearshore and coastal regions (Dietrich et al., 2010; Weisberg and Zheng, 2006).

The transport of drifting objects or substances that are locally released is often best represented by a Lagrangian individual-based model. Such an approach is routinely used to model the dispersal of larvae, pollutants, sediments and many other tracers (e.g. Le Hénaff et al., 2012; Liubartseva et al., 2018; Figueiredo et al., 2013; Frys et al., 2020). Although some transport models take the impact of waves into account by adding a Stokes drift velocity, *i.e.* the net drift of a floating particle in the direction of the wave propagation (Van Den Bremer and Breivik, 2018), to the Eulerian currents, they usually neglect the wave-induced currents. Such practice is reasonable in fair weather, when wave-induced forces exerted on currents are relatively small, but may lead to significant errors during storm conditions (Röhrs et al., 2012; Curcic et al., 2016).

51 The objective of this study is therefore to assess the importance of wave-  
52 current interactions during a tropical cyclone. We investigate the transport  
53 of drifting particles on the Florida shelf during Hurricane Irma, one of the  
54 strongest and costliest tropical cyclones on record in the Atlantic Basin (Xian  
55 et al., 2018), which made landfall in Florida in September 2017. To do  
56 that, we developed an unstructured-mesh coupled wave-current model of  
57 South Florida to simulate the ocean circulation under hurricane conditions.  
58 Both modeled currents and waves were validated against field measurements  
59 and then used to simulate the transport of drifting material in the Florida  
60 Keys and the Florida inner shelf. Model outputs were then compared with  
61 uncoupled simulation results in order to assess the impact of wave-induced  
62 forces and Stokes drift on the modeled currents and transports.

63 **2. Methods**

64 *2.1. Study area and observational data*

65 The large-scale ocean circulation around South Florida is dominated by  
66 the Florida Current (FC), which originates from the Loop Current (LC) where  
67 it enters the Florida Straits from the Gulf of Mexico, and, downstream, forms  
68 the Gulf Stream. The FC is a major western boundary current characterized  
69 by spatial variability and meandering, associated with the presence of cyclonic  
70 eddies between the core of the current and the complex reef topography  
71 of the Florida Reef Tract (FRT) (Lee et al., 1995; Kourafalou and Kang,  
72 2012). The variability of the FC extends over a large range of spatial and  
73 temporal scales, with periods of 30-70 days in the Lower Keys (Lee et al., 1995)  
74 and shorter periods of 2-21 days in the Upper Keys (Lee and Mayer, 1977),  
75 and exhibits significant seasonal and interannual cycles (Johns and Schott,  
76 1987; Lee and Williams, 1988; Schott et al., 1988). Circulation on the West  
77 Florida Shelf (WFS), on the other hand, is forced by local winds and tidal  
78 fluctuations (Lee and Smith, 2002; Liu and Weisberg, 2012). Furthermore,  
79 due to its location relative to the warm waters of the North Atlantic, Florida

80 is particularly vulnerable to tropical cyclones. On average, the state gets  
81 hit by a hurricane every two years and strong hurricanes, some of which are  
82 among the most destructive on record, strike Florida on average once every  
83 four years (Malmstadt et al., 2009).

84 The state of the ocean around Florida is monitored by an extensive  
85 array of tide gauges, current meters and buoys. In this study, we used sea  
86 surface elevation measurements from the National Oceanic and Atmospheric  
87 Administrations (NOAA) Tides and Currents dataset. These measurements  
88 were taken at four locations: two in the Florida Keys (Key West and Vaca  
89 Key); one on the East coast of Florida (Virginia Key); and one on the West  
90 coast (Naples). For the currents, we used ADCP measurements from the  
91 University of South Florida's College of Marine Science's (USF/CMS) Coastal  
92 Ocean Monitoring and Prediction System (COMPS) for the WFS (Weisberg  
93 et al., 2009). More specifically, we used measurements from moorings C10,  
94 C12 and C13, respectively located at the 25, 50, and 50 m isobaths of the  
95 WFS (Liu et al., 2020). Finally, for the waves, we used measurements from  
96 four buoys of the NOAA's National Data Buoy Center (NDBC); two on  
97 Florida's eastern shelf and two on the WFS. The locations of all measurement  
98 stations are shown in Fig. 1A,C.

99 *2.2. Wind and atmospheric pressure during Hurricane Irma*

100 Hurricane Irma made landfall in Florida on 10 September 2017 as a  
101 category 3 hurricane, first at Cudjoe Key (Florida Keys) and later on Marco  
102 Island, south of Naples (see hurricane track in Fig. 1). It then weakened to a  
103 category 2 hurricane as it moved further inland (Pinelli et al., 2018). The  
104 storm damaged up to 75% of the buildings at its landfall point in the Florida  
105 Keys, making it one of the strongest and costliest hurricanes on record in the  
106 Atlantic basin (Xian et al., 2018; Zhang et al., 2019). The strongest reported  
107 wind speed was 50 m/s on Marco Island while the highest recorded storm  
108 surge was 2.3 m, although larger wind speed likely occurred in the Florida  
109 Keys (Pinelli et al., 2018). To reproduce the wind profile of Irma in our model,

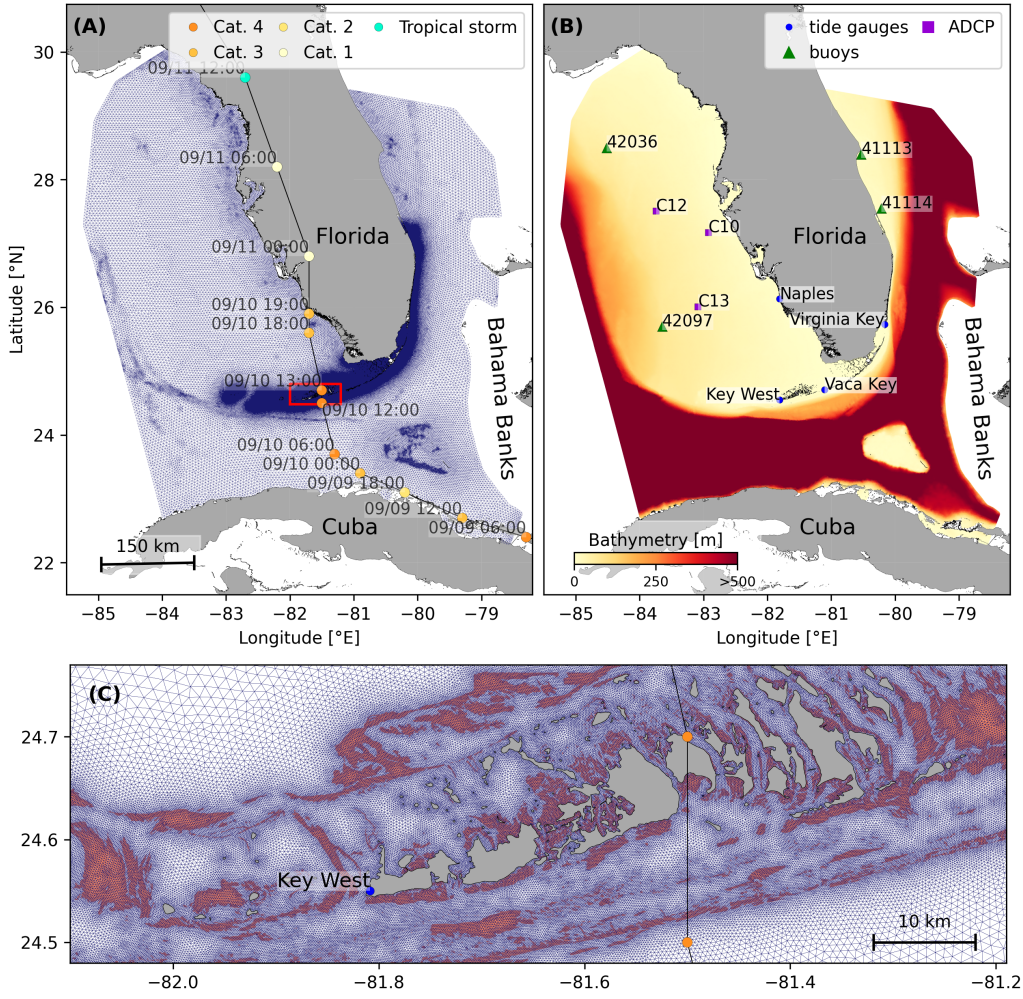


**Fig. 1:** (A) Mesh of the computational domain with the trajectory of Irma. The category of the hurricane is given by the Saffir-Simpson color scale. (B) Bathymetry of the domain with the location of stations used for the validation of the model outputs. (C) Close up view of the Lower Keys area, where the mesh resolution reaches 100 m near reefs (shown in dark orange) and islands (highlighted in dark grey)

we used high-resolution H\*Wind wind fields (Powell et al., 1998). As these data represent 1-min averaged wind speeds, we multiplied them by a factor 0.93 to obtain 10-min averaged wind speeds (Harper et al., 2010), which are more consistent with the time step of our model. Furthermore, H\*Wind wind profiles did not cover the whole model extent during the passage of the hurricane and were thus blended within coarser wind field extracted from ECMWF ERA-5 datasets (Fig. 2A). The pressure field during the passage of Hurricane Irma was also reconstructed using ERA-5 data. However, the coarse resolution of the dataset smoothes out the depression at the center of the hurricane, leading to an underestimation of the pressure gradient (Fig. 2B). To better capture the central depression of Irma, we therefore built a hybrid pressure field using the position and the minimal pressure of the core of the hurricane based on its track as recorded in the HURDAT 2 database (Landsea and Franklin, 2013). Based on this information, the hybrid pressure field was constructed by combining an idealized Holland pressure profile (Lin and Chavas, 2012) within the radius of maximum wind speed of Irma (Knaff et al., 2018) with ERA-5 pressure field. The transition from the Holland profile to ERA-5 data outside the radius of maximum wind speed data was performed using a smooth step function (Fig. 2).

### 2.3. Hydrodynamic model

Ocean currents generated during hurricane Irma around South Florida were modeled using the 2D barotropic version of the unstructured-mesh coastal ocean model SLIM<sup>1</sup> (Lambrechts et al., 2008). The model mesh covers an area similar to the model extent of Dobbelaere et al. (2020), that includes the FRT but also the Florida Straits and part of the Gulf of Mexico (Figure 1). However, this area has been slightly extended northeastward and westward in order to include the NOAA-NDBC buoys. Furthermore, to withstand potential cell drying during the hurricane, we solved the conservative shallow

---

<sup>1</sup><https://www.slim-ocean.be>

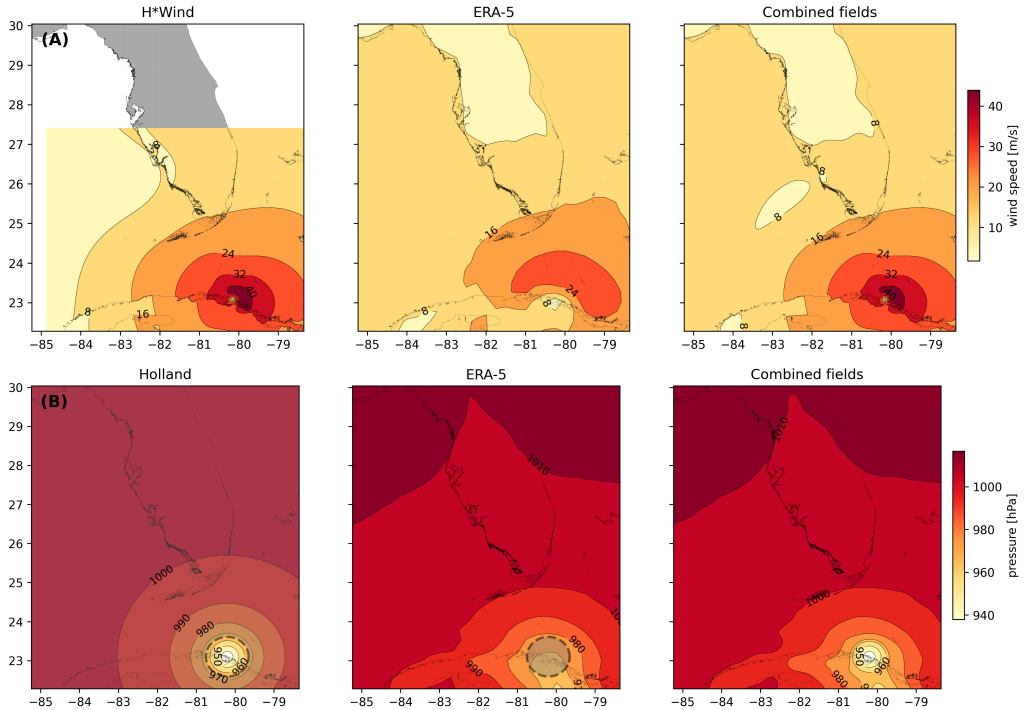


**Fig. 2:** Snapshot of the hybrid wind (A) and pressure (B) profiles constructed to capture the passage of Hurricane Irma at 1800 UTC on 9 September 2017. Wind profiles are obtained by combining high resolution H\*Wind with coarser ERA-5 wind fields. The pressure field is built by combining the ERA-5 pressure field with an idealized Holland pressure profile based on the track of Irma in the HURDAT 2 database. Holland field was only used within the radius of maximum wind speed (dashed grey line) of the hurricane to capture its central depression.

<sub>138</sub> water equations with wetting-drying:

$$\begin{aligned} \frac{\partial H}{\partial t} + \nabla \cdot (\mathbf{U}) &= 0, \\ \frac{\partial \mathbf{U}}{\partial t} + \nabla \cdot \left( \frac{\mathbf{U}\mathbf{U}}{H} \right) + f\mathbf{e}_z \times \mathbf{U} &= \alpha g H \nabla(H - h) - \frac{1}{\rho} \nabla p_{\text{atm}} + \frac{1}{\rho} \boldsymbol{\tau}_s \\ &\quad + \nabla \cdot (\nu \nabla \mathbf{U}) - \frac{C_b}{H^2} |\mathbf{U}| \mathbf{U} + \gamma (\mathbf{U}_{\text{ref}} - \mathbf{U}), \end{aligned} \quad (1)$$

<sub>139</sub> where  $H$  is the water column height and  $\mathbf{U}$  is the depth-averaged transport;  
<sub>140</sub>  $f$  is the Coriolis coefficient;  $g$  is the gravitational acceleration;  $h$  is the  
<sub>141</sub> bathymetry;  $\alpha$  is a coefficient indicating whether the mesh element is wet  
<sub>142</sub> ( $\alpha = 1$ ) or dry ( $\alpha = 0$ ) (Le et al., 2020);  $\nu$  is the viscosity;  $C_b$  is the  
<sub>143</sub> bulk bottom drag coefficient;  $p_{\text{atm}}$  is the atmospheric pressure;  $\boldsymbol{\tau}_s$  is the  
<sub>144</sub> surface stress, usually due to wind; and  $\gamma$  is a relaxation coefficient towards a  
<sub>145</sub> reference transport  $\mathbf{U}_{\text{ref}}$ . As in Frys et al. (2020) and Dobbelaere et al. (2020),  
<sub>146</sub> SLIM currents were gradually relaxed towards the operational Navy HYCOM  
<sub>147</sub> product (GOMl0.04<sup>2</sup>, Chassignet et al. (2007)) in regions where the water  
<sub>148</sub> depth exceeds 50m.

<sub>149</sub> At very high wind speeds, the white cap is blown off the crest of the  
<sub>150</sub> waves. This phenomenon, also known as spume, has been hypothesized to  
<sub>151</sub> generate a layer of droplets that acts as a slip layer for the winds at the  
<sub>152</sub> ocean-atmosphere interface (Holthuijsen et al., 2012). It causes a saturation  
<sub>153</sub> of the wind drag coefficient for strong winds (Powell et al., 2003; Donelan  
<sub>154</sub> et al., 2004; Curcic and Haus, 2020). We take this saturation effect into  
<sub>155</sub> account by using the wind drag parameterization of Moon et al. (2007). In  
<sub>156</sub> this parameterization, the drag coefficient  $C_d$  depends on the wind speed at

---

<sup>2</sup><https://www.hycom.org/data/goml0pt04>

<sub>157</sub> 10-m height  $U_{10}$  according to:

$$C_d = \kappa^2 \log \left( \frac{10}{z_0} \right)^{-2} \quad (2)$$

<sub>158</sub> where  $\kappa$  is the von Karman constant and  $z_0$  is the roughness length expressed  
<sub>159</sub> as:

$$z_0 = \begin{cases} \frac{0.0185}{g} u_*^2 & \text{if } U_{10} \leq 12.5 \text{ m/s ,} \\ [0.085(-0.56u_*^2 + 20.255u_*) + 2.458] - 0.58] \times 10^{-3} & \text{if } U_{10} > 12.5 \text{ m/s ,} \end{cases} \quad (3)$$

<sub>160</sub> with  $u_*$  the friction velocity. The relation between  $U_{10}$  and  $U_*$  is given by:

$$U_{10} = -0.56u_*^2 + 20.255u_* + 2.458 . \quad (4)$$

<sub>161</sub> The mesh resolution depends on the distance to the coastlines and reefs  
<sub>162</sub> following the approach of Dobbelaere et al. (2020). The mesh is then further  
<sub>163</sub> refined according to bathymetry value and gradient, as suggested in the  
<sub>164</sub> SWAN user-guide<sup>3</sup>. Such an approach improves the model efficiency as the  
<sub>165</sub> mesh resolution is only increased where required by the currents and waves  
<sub>166</sub> dynamics. The mesh was generated with the seamsh<sup>4</sup> Python library, which is  
<sub>167</sub> based on the open-source mesh generator GMSH (Geuzaine and Remacle,  
<sub>168</sub> 2009). It is composed of approximately  $7.7 \times 10^5$  elements. The coarsest  
<sub>169</sub> elements, far away from the FRT, have a characteristic length of about 5 km  
<sub>170</sub> whereas the finest elements have a characteristic length of about 100 m along  
<sub>171</sub> the coastlines and over the reefs (Fig 1).

<sub>172</sub> *2.4. Wave model*

<sub>173</sub> Waves were modeled using the parallel unstructured-mesh version of the  
<sub>174</sub> Simulating WAves Nearshore (SWAN) model (Booij et al., 1999), one of the

---

<sup>3</sup><http://swanmodel.sourceforge.net/unswan/unswan.htm>

<sup>4</sup><https://pypi.org/project/seamsh/>

175 most popular wave models for coastal areas and inland waters. It solves the  
176 action balance equation (Mei, 1989):

$$\frac{\partial N}{\partial t} + \nabla_{\mathbf{x}} \cdot [(\mathbf{c}_g + \mathbf{u})N] + \frac{\partial}{\partial \theta}[c_\theta N] + \frac{\partial}{\partial \sigma}[c_\sigma N] = \frac{S_{in} + S_{ds} + S_{nl}}{\sigma}, \quad (5)$$

177 where  $N = E/\sigma$  is the wave action density and  $E$  is the wave energy spectrum;  
178  $\theta$  is the wave propagation direction;  $\sigma$  is the intrinsic wave frequency;  $\mathbf{c}_g$  is  
179 the wave group velocity,  $\mathbf{u} = \mathbf{U}/H$  is SLIM depth-averaged current velocity;  
180  $c_\theta$  and  $c_\sigma$  are the propagation velocities in spectral space due to refraction  
181 and shifting in frequency due to variations in depth and currents; and  $S_{in}$ ,  
182  $S_{ds}$ , and  $S_{nl}$  respectively represent wave growth by wind, wave decay and  
183 nonlinear transfers of wave energy through interactions between triplets and  
184 quadruplets. The wave spectra were discretized with 48 direction bins and 50  
185 frequency bins logarithmically distributed from 0.03 to 2 Hz. Exponential  
186 wind growth was parameterized using the formulation of Janssen (1991), while  
187 dissipations by whitecapping and bottom dissipation followed the formulations  
188 of Komen et al. (1984) and Madsen et al. (1989), respectively.

189 Coefficients for exponential wind growth and whitecapping parameteriza-  
190 tions were based on the results of Siadatmousavi et al. (2011), and significantly  
191 differ from SWAN's default settings. By default, SWAN implements the wind  
192 input formulation of Komen et al. (1984) and the steepness-dependent co-  
193 efficient governing dissipation by whitecapping is a linear function of the  
194 wavenumber. In this study, this steepness-dependent coefficient is a quadratic  
195 function of the wavenumber, as it showed better predictions of the significant  
196 wave height in the study of Siadatmousavi et al. (2011). The choice of these  
197 formulations was motivated by the appearance of numerical instabilities in  
198 the region of the Gulf Stream when using SWAN's default parameter values.  
199 Finally, wave boundary conditions were derived from WAVEWATCH III  
200 (Tolman et al., 2009) spectral outputs at NDBC buoy locations. We selected  
201 these datasets as the large number of NDBC buoys around our region of  
202 interest allowed for a fine representation of the wave spectra on the boundary

203 of the domain.

204 Surface waves induce a net drift in the direction of the wave propagation,  
205 known as the Stokes drift (Van Den Bremer and Breivik, 2018; Stokes,  
206 1880). This net drift has a significant impact on sediment transport in  
207 nearshore regions (Hoefel and Elgar, 2003), on the formation of Langmuir  
208 cells (Langmuir, 1938; Craik and Leibovich, 1976) as well as on the transport  
209 of heat, salt or pollutants such as oil or micro-plastic in the upper ocean layer  
210 (McWilliams and Sullivan, 2000; Röhrs et al., 2012; Drivdal et al., 2014). To  
211 correctly model the Stokes drift profile in mixed wind-driven sea and swell  
212 conditions, the full two-dimensional wave spectrum must be represented by a  
213 spectral wave model within a wave-current coupling (Van Den Bremer and  
214 Breivik, 2018). We therefore used SWAN modeled spectra to compute the  
215 Stokes drift as follows:

$$\mathbf{u}_s = \int_0^{2\pi} \int_0^{+\infty} \frac{\sigma^3}{h \tanh(2kh)} E(\sigma, \theta) (\cos \theta, \sin \theta) d\sigma d\theta , \quad (6)$$

216 where  $k$  is the norm of the wave vector;  $h$  is the water depth; and  $E(\sigma, \theta)$  is  
217 the wave energy density.

### 218 2.5. Coupled model

219 SLIM and SWAN are coupled so that they run on the same computational  
220 core and the same unstructured mesh. SLIM is run first and passes the  
221 wind velocity ( $\mathbf{U}_{10}$ ), water level ( $\eta = H - h$ ) and depth-averaged current  
222 ( $\mathbf{u} = \mathbf{U}/H$ ) fields to SWAN, as well as a roughness length ( $z_0$ ) for the bottom  
223 dissipation formulation of Madsen et al. (1989). This roughness length is  
224 computed from SLIM's bulk drag coefficient  $C_b$  following the approach of  
225 Dietrich et al. (2011) so that both models have consistent bottom dissipation  
226 parameterizations. SWAN then uses these quantities to compute the wave  
227 radiation stress gradient, that is then passed to SLIM as the force exerted  
228 by waves on currents  $\boldsymbol{\tau}_{\text{wave}}$  (Fig. 3). SLIM then uses this quantity to  
229 update the value of the surface stress  $\boldsymbol{\tau}_s$  in Eq. (1), that now becomes

the sum of wind and wave-induced stresses  $\tau_s = \tau_{\text{wind}} + \tau_{\text{wave}}$ . Here, the momentum flux from the atmosphere to the ocean is taken as the commonly used full wind stress  $\tau_{\text{wind}}$ . Doing so, we neglect the momentum advected away from the storm by the waves, leading to a 10-15% overestimation of the momentum flux in hurricane winds (Curcic, 2015). Moreover, we followed the approach of Dietrich et al. (2012) by characterizing the wave-induced stresses using the radiation-stress representation instead of the vortex-force representation (McWilliams et al., 2004). Although the latter provides a clearer and more meaningful decomposition of the wave effect, we implemented the first representation for the sake of simplicity as it allows us to provide the whole wave contribution as an additional surface stress to SLIM (Lane et al., 2007).

SLIM's governing equations are integrated using an implicit time integration scheme while SWAN is unconditionally stable (Dietrich et al., 2012), allowing both models to be run with relatively large time steps. In this study, the stationary version of SWAN was used, *i.e.* the time derivative of Eq. (5) was set to zero. This resulted in reduced scaling and convergence rates than with the nonstationary version of SWAN but increased the stability of the model. The wave spectra at each node of the mesh was saved at the end of each iteration to serve as initial conditions for the next one. Both models were run sequentially using a time step of 600 s, so that each computational core was alternatively running either SLIM or SWAN. As in the coupling between SWAN and ADCIRC (Dietrich et al., 2012), both models use the same local sub-mesh, allowing for a one-to-one correspondence between the geographic locations of the mesh vertices. No interpolation is therefore needed when passing the discretised variables from one model to the other, which allows an efficient inter-model communication. However, as SLIM is based on a discontinuous Galerkin finite element method, an additional conversion step to a continuous framework was required to transfer SLIM nodal quantities to SWAN.

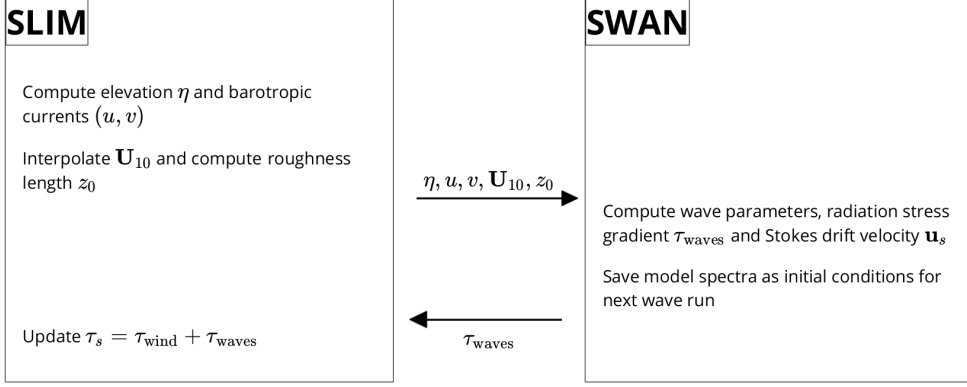


**Fig. 3:** Schematic illustration of the coupled SLIM+SWAN model.

260    *2.6. Quantifying the effect of wave-current interactions on transport*

261    To quantify the impact of wave-current interactions on transport processes,  
 262    we compared the trajectories of passive particles advected by the uncoupled  
 263    SLIM and coupled SLIM+SWAN currents during the passage of Irma in the  
 264    Lower Keys. Furthermore, the depth-averaged Stokes drift was computed  
 265    using the wave spectra of the coupled model SLIM+SWAN run as well as  
 266    those of an uncoupled SWAN run. Particles were released on the inner and  
 267    outer shelves at the points highlighted by red and blue dots in Fig. 4 on  
 268    Sept. 7 at 0000 UTC and then tracked until Sept. 15. These initial particle  
 269    positions were found using backtracking methods (Spivakovskaya et al., 2005)  
 270    to ensure that the release particles would intersect the path of Irma during  
 271    its passage through the Florida Keys. We first defined two 25 km<sup>2</sup> circular  
 272    regions on the trajectory of the hurricane (see red and blue circles in Fig. 4).  
 273    Particles within these two regions were then tracked backward in time using  
 274    uncoupled SLIM currents from the exact time of the passage of the hurricane  
 275    until Sept. 7 at 0000 UTC. Their positions at the end of the backward  
 276    simulation (see red and blue particle clouds in Fig. 4) corresponds to the  
 277    initial condition of the forward transport simulations described below. We  
 278    then compared the trajectories of particles originating from these regions and

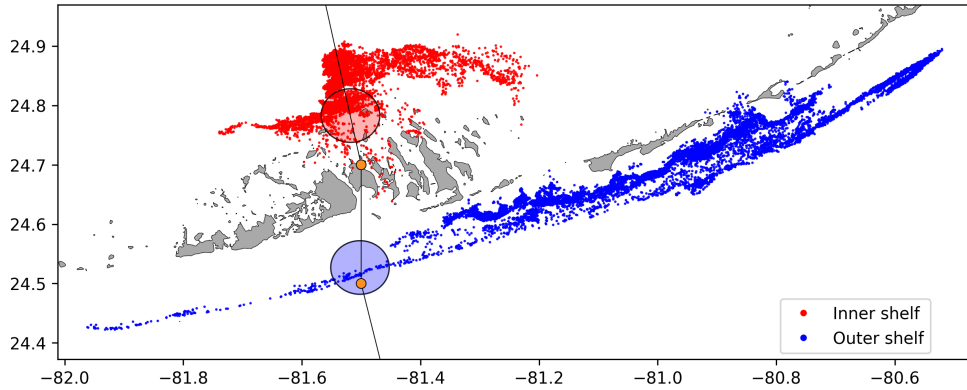


**Fig. 4:** Release regions of the passive particles on the inner and outer shelves (red and blue clouds) obtained by backtracking particles released in the red and blue circular areas during the passage of Irma.

advedted forward in time by different sets of currents: (i) uncoupled SLIM currents alone; (ii) coupled SLIM+SWAN currents; (iii) SLIM currents with the addition of the depth-averaged Stokes drift computed with the coupled wave-current model (Stokes-C); (iv) SLIM+SWAN currents with Stokes-C; and (v) SLIM currents with the depth-averaged Stokes drift computed with the uncoupled wave model (Stokes-U). Particle trajectories are compared by computing the distances between the centers of mass of the particle clouds through time.

### 3. Results

We first validated the reconstructed atmospheric fields of hurricane Irma as well as the outputs of our coupled wave-current model against field measurements. We then used the validated model outputs to simulate the transport of passive drifters in the Lower Keys during the passage of Hurricane Irma. These drifters were advected by the sets of currents described in section 2.6 and their trajectories were compared to evaluate the impact of the wave-current interactions and the Stokes drift on the transport processes during the passage of Irma.

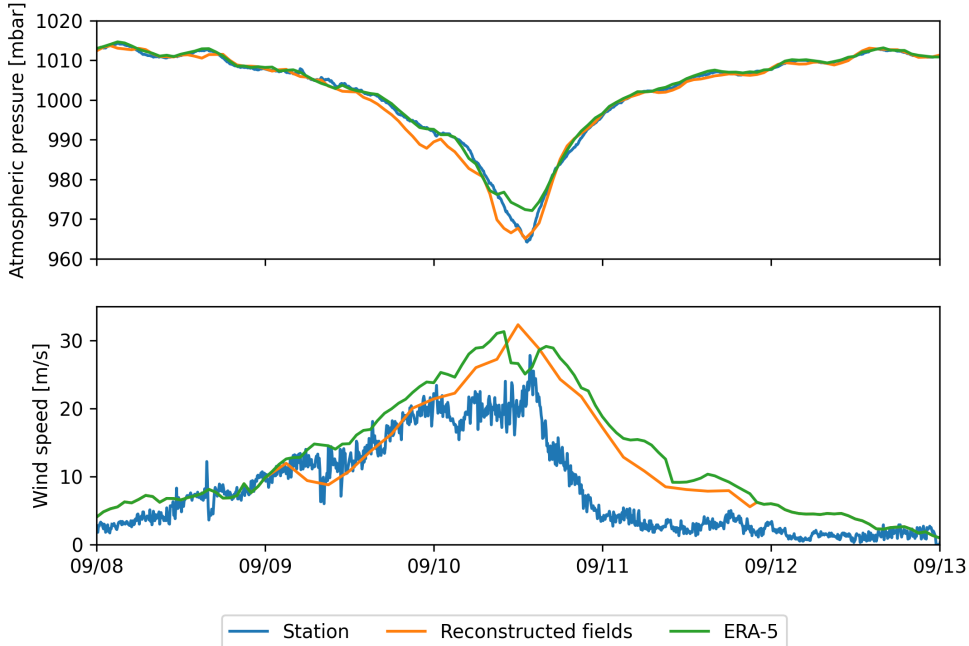


**Fig. 5:** Comparison of reconstructed wind atmospheric pressure with field measurements and coarser ECMWF ERA-5 profiles at Vaca Key station. The generated hybrid atmospheric forcings better reproduce the observed storm depression while H\*wind winds better reproduce the measured peak in wind speed.

296     3.1. *Model validation*

297     H\*Wind winds and hybrid pressure field agree well with station mea-  
 298     surements at Vaca Key station (Fig. 5). The hybrid pressure field shows a  
 299     better agreement with observations than ERA-5 pressure as it successfully  
 300     reproduces the storm depression. ERA-5 fields, on the other hand, fail to  
 301     reproduce the low pressure at the core of the hurricane due to their coarser  
 302     grid, leading to an overestimation of 8 mbar of the storm depression. Both  
 303     H\*Wind and ERA-5 agree well with observed wind speeds although both  
 304     data sets tend to slightly overestimate the width and intensity of the wind  
 305     peak. However, H\*wind profiles better reproduce the timing of the observed  
 306     peak, as ERA-5 winds tend to anticipate it. H\*wind also exhibits a slightly  
 307     narrower peak in wind speed, which better agrees with observations.

308 Hydrodynamic outputs of the coupled wave-current model agree well with  
309 tide gauge (Fig. 6) and ADCP measurements (Fig. 7). Despite a slight  
310 overestimation of the amplitude of sea surface elevation (Table 1) in fair  
311 weather conditions, the timing and amplitude of the storm surges are well  
312 reproduced by the coupled model. The largest model error during the surge  
313 is an overestimation of 18 cm of the elevation peak at Virginia Key. The fit is  
314 especially good at Naples, where both the large positive and negative surges  
315 are captured by the coupled model with an error of less than 5 cm. modeled  
316 2D currents were validated against depth-averaged ADCP measurements  
317 at mooring stations C10, C12 and C13 (Fig. 7). As in Liu et al. (2020),  
318 we performed the vector correlation analysis of Kundu (1976) to compare  
319 modeled and observed current velocity vectors. Correlation coefficients ( $\rho$ )  
320 between simulated and observed depth-averaged currents are 0.84, 0.74 and  
321 0.73 at stations C10, C12 and C13, respectively. The average veering angles  
322 are below 12°, as in (Liu et al., 2020). Furthermore, the positive bias in Table  
323 1 indicates that our model tends to underestimate the southward component  
324 of the currents at the different stations. As expected from a depth-averaged  
325 model, the best fit with observations is obtained at the shallowest mooring  
326 C10, located on the 25 m isobath, with an average veering angle of 6° and  
327 smaller error statistics (Table 1).

328 The simulated significant wave height agrees well with observations on  
329 the WFS, where errors on the peak value do not exceed 5% (Fig. 8). On  
330 Florida's eastern shelf, errors are slightly larger and reach 20%. Although the  
331 model outputs agree well with observations, a lag in significant wave height is  
332 observed for all 4 buoys. Moreover, the peak in significant wave height tends  
333 to be underestimated at buoys 41113 and 41114, located on the eastern shelf  
334 of Florida. The same tendency is observed with the modeled wave period,  
335 with mean errors inferior to 1 second on the WFS and reaching more than  
336 2 seconds on Florida's eastern shelf (Table 1), as the coupled model fails  
337 to reproduce the observed peak in wave period between the 7th and 8th of

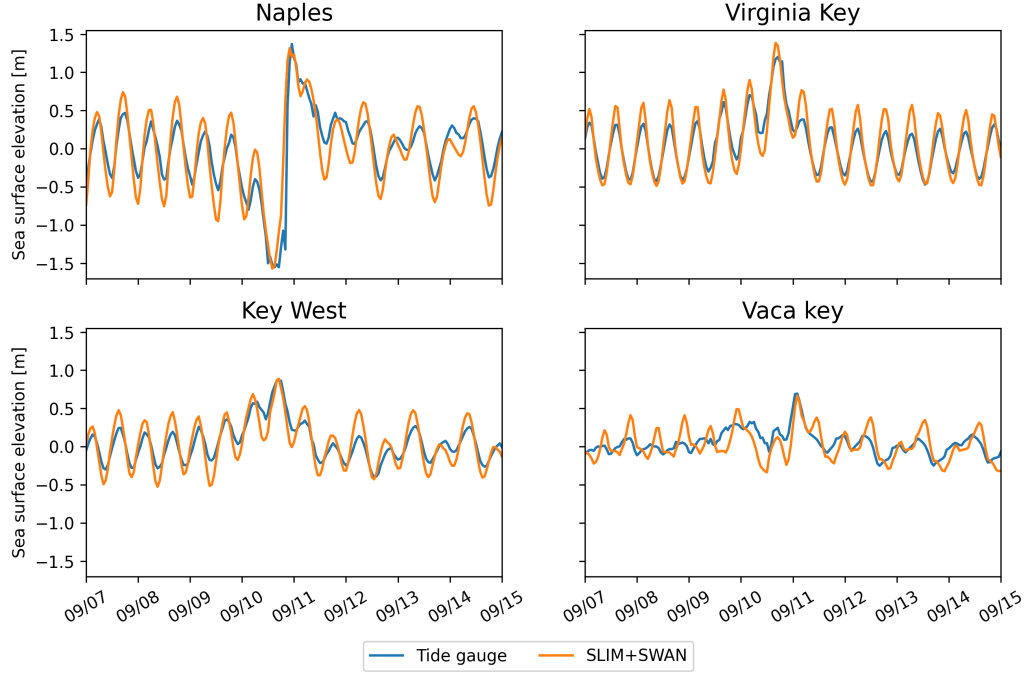


**Fig. 6:** Comparison of modeled sea surface elevation at the 4 tide gauges shown in Fig. 1B. The timing and amplitudes of the storm surges are well reproduced by the model

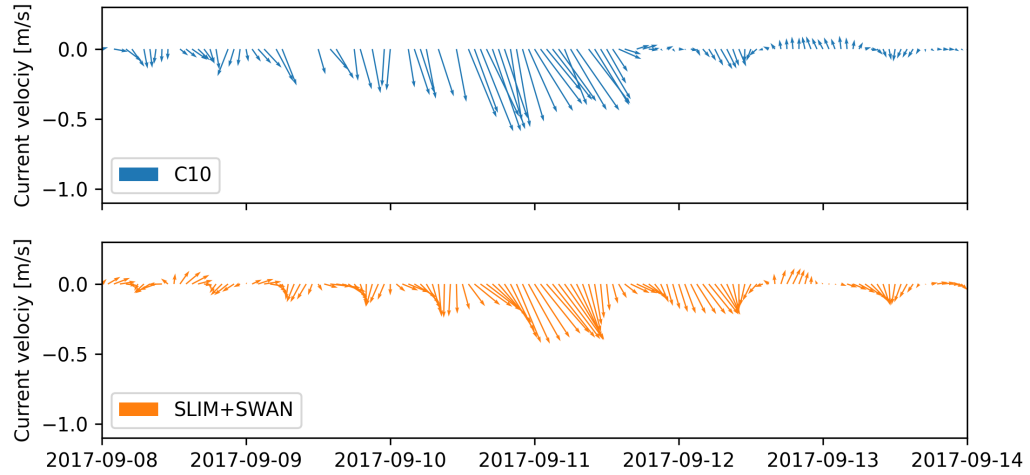


**Fig. 7:** Comparison of modeled current velocity with observed velocity at mooring C10 (see Fig. 1B for its location). modeled current velocities agree well with observations, with a correlation coefficient of 0.83 and an average veering angle of 6°.

338 September on this side of Florida. Finally, modeled wave direction agrees well  
339 with observation (Fig. 8), although our model tends to overestimate wave  
340 propagation in the northward direction at stations 41114 and 41113 on the  
341 passage of the hurricane.

342 *3.2. Impact of waves on currents and transport*

343 We evaluated the impact of wave-current interactions on modeled currents  
344 during the passage of Irma in the Lower Keys, between Sept. 7 and 13, 2017.  
345 First, we computed the maximum difference between currents modeled by  
346 SLIM and SLIM+SWAN during this period (Fig. 9A). The largest differences  
347 in current speed were observed over the reefs, on the shelf break and around  
348 islands. They locally reach 1 m/s, with the coupled SLIM+SWAN model  
349 yielding the largest amplitudes. The regions where the differences are the  
350 largest experience the strongest radiation-stress gradient  $\tau_{\text{wave}}$  (Fig. 9B)  
351 induced by wave energy dissipation on the shelf-break and rough seabed  
352 induce variations of the wave radiation stress (Longuet-Higgins and Stewart,  
353 1964). This highlights the important protective role of the barrier formed  
354 by the offshore reefs, that require a fine spatial resolution to be accurately  
355 captured. Wave-induced differences in current speed were amplified by the  
356 action of the wind stress  $\tau_{\text{wind}}$  (Fig. 9C). Wind speeds were larger in the front  
357 right quadrant of the hurricane (Zedler et al., 2009), yielding larger differences  
358 on the right-hand side of the storm trajectory. This is especially clear in the  
359 area between the Florida Keys and the Everglades, where relatively small  
360 values of  $\tau_{\text{wave}}$  nonetheless produce current speed differences of up to 0.5 m/s  
361 because of the wind stress.

362 Waves play a significant role on the transport processes during and after the  
363 passage of hurricane Irma (Fig. 10A,B). Comparing SLIM and SLIM+SWAN  
364 shows that wave-current interactions alone yield differences of up to 5 km  
365 between the modeled trajectories on the passage of the hurricane. These  
366 differences exceed 10 km on the outer shelf when Stokes drift is taken into  
367 account. Such deflections are not negligible when compared to the total

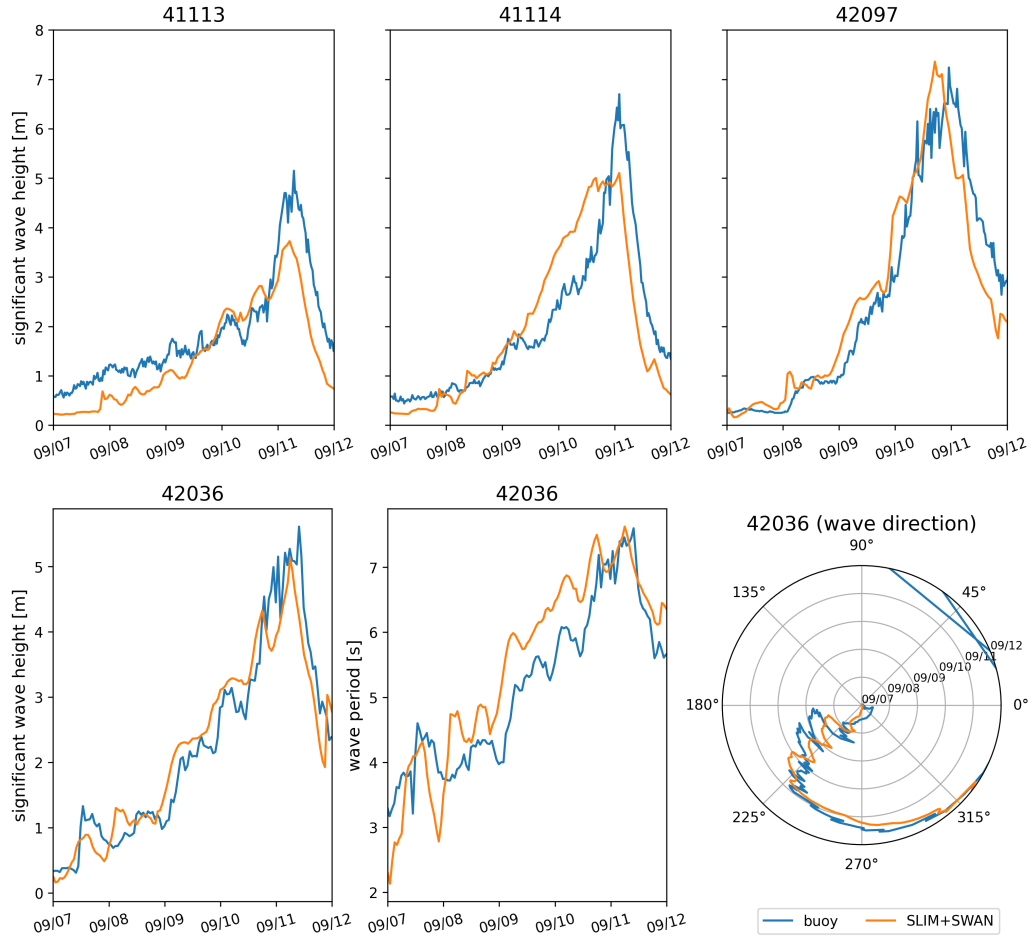


**Fig. 8:** Comparison of modeled wave parameters with observation at the 4 buoys location (locations shown in Fig. 1B). The modeled significant wave heights agree well with field measurement.

<b>Station</b>	<b>Variable</b>	<b>Bias</b>	<b>MAE</b>	<b>RMSE</b>
Vaca Key	sse (m)	n/a	0.12	0.16
	$U_{10}$ (m/s)	1.51	1.85	2.61
	$p_{\text{atm}}$ (hPa)	-0.21	0.59	1.03
Key West	sse (m)	n/a	0.11	0.13
Virginia Key	sse (m)	n/a	0.10	0.13
Naples	sse (m)	n/a	0.18	0.23
C10	$u$ (m/s)	-0.006	0.04	0.05
	$v$ (m/s)	0.02	0.06	0.08
C12	$u$ (m/s)	-0.01	0.06	0.07
	$v$ (m/s)	0.06	0.09	0.11
C13	$u$ (m/s)	0.004	0.06	0.08
	$v$ (m/s)	0.04	0.06	0.08
41113	$H_s$ (m)	-0.35	0.40	0.51
	$T_m$ (s)	-2.18	2.47	3.13
	$\theta_m$ (degree)	7.17	19.50	26.06
41114	$H_s$ (m)	-0.21	0.53	0.68
	$T_m$ (s)	-1.69	2.53	3.15
	$\theta_m$ (degree)	31.25	35.28	46.18
42036	$H_s$ (m)	-0.03	0.26	0.36
	$T_m$ (s)	0.04	0.65	0.77
	$\theta_m$ (degree)	19.92	30.65	41.69
42097	$H_s$ (m)	-0.15	0.40	0.57
	$T_m$ (s)	0.02	0.62	0.74
	$\theta_m$ (degree)	3.62	28.08	45.89

Table 1: Error statistics on the wave-current model outputs as compared to the measured sea surface elevation (sse), eastward and northward depth-average current velocities ( $u,v$ ), significant wave height ( $H_s$ ), zero-crossing mean wave period ( $T_m$ ) and mean wave direction ( $\theta_m$ ). Model bias, mean absolute error (MAE), and root mean squared error (RMSE) are listed by variable (unit) and value.

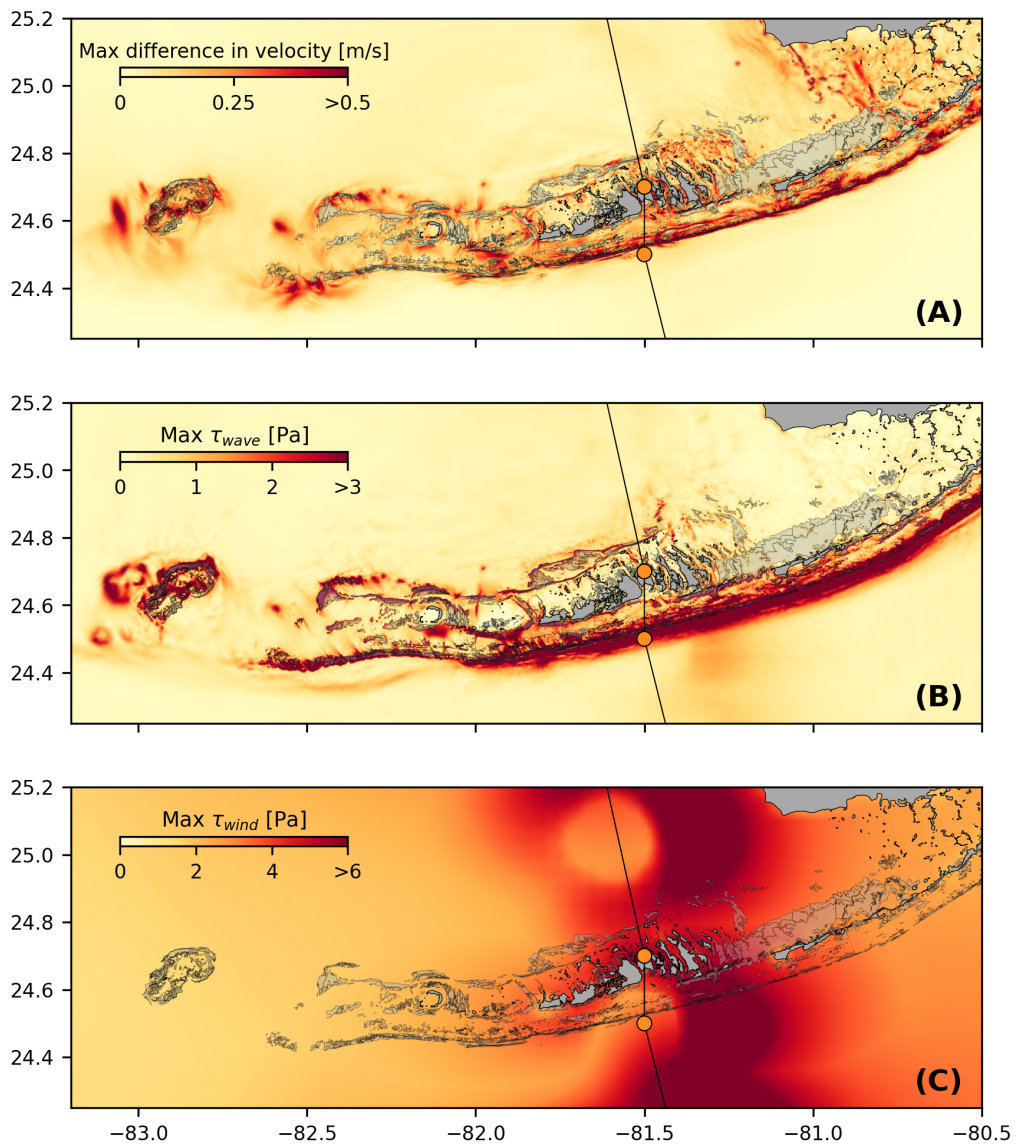


**Fig. 9:** (A). Maximum difference between SLIM and SLIM+SWAN currents during the passage of Irma in the Lower Florida Keys; (B) Maximum wave radiation stress gradient  $\tau_{wave}$  and (C) maximum wind stress  $\tau_{wind}$  (C) generated by the hurricane. Radiation stress gradient yields difference larger than 0.5 m/s (and locally reaching 1m/s) in current velocities, especially over offshore reefs.

368 distance traveled by particle clouds. For all simulations, modeled particles  
369 were transported up to 30 km from their release point on the inner shelf  
370 and up to 60 km on the outer shelf. The impact of the waves on the  
371 transport processes differs significantly between the inner and outer shelves,  
372 with wave-induced differences in trajectories 4 to 5 times larger on the outer  
373 shelf. Furthermore, the distance between the centers of mass of the clouds  
374 of particles tends to stabilize on the inner shelf after the passage of Irma,  
375 while it keeps increasing on the other shelf up to two days after the passage  
376 of the hurricane when taking Stokes drift into account. The distance then  
377 stabilizes for about a day before it starts decreasing (see right panel of Fig.  
378 10A,B). However, when considering wave-current interactions alone (SLIM  
379 vs. SLIM+SWAN), the distance between the clouds of particles starts to  
380 decrease just after the passage of Irma.

381 The Stokes drift appears to have a larger effect than the radiation stress  
382 gradient and the wave-current interactions (Fig 10A,B). Nonetheless, compar-  
383 ing the different curves for the outer shelf suggests that the radiation-stress  
384 gradient induces effects similar to the impact of the Stokes drift in this  
385 region during the passage of Irma. However, when comparing SLIM and  
386 SLIM+SWAN both on the inner and other shelf, this impact appears to be  
387 negligible during the rest of the simulation. Comparing Stokes-U and Stokes-C  
388 indicates that the difference between the trajectories of particles advected by  
389 the two Stokes drifts does not exceed 2 km, with larger discrepancies on the  
390 outer shelf (Fig. 10C,D). The distance between the two clouds of particles  
391 increases abruptly on the passage of the hurricane (and two days after on the  
392 outer shelf) and then stabilizes during the rest of the simulation.

#### 393 4. Discussion

394 The coupled SLIM+SWAN model correctly reproduces the hydrodynamics  
395 and wave dynamics during hurricane Irma. Such good agreement with field  
396 measurements can only be achieved using accurate forcings and adequate

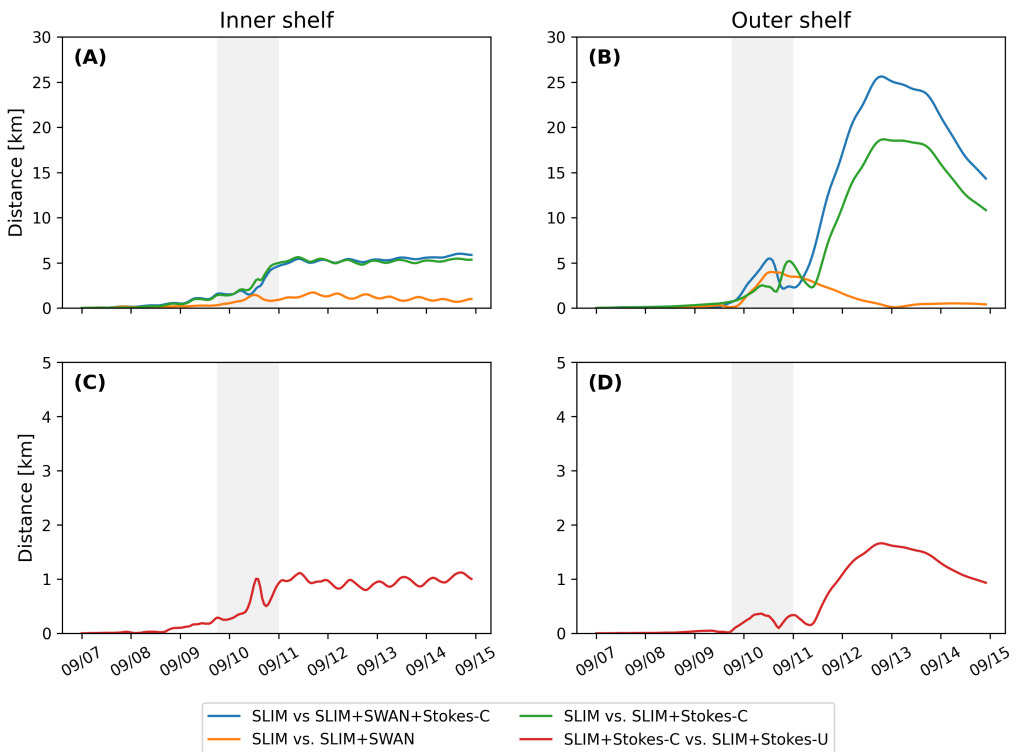


**Fig. 10:** Difference between the centers of mass of the particle clouds released from the regions highlighted in Fig. 4 and advected by different combinations of coupled and uncoupled velocity fields.

397 wave parameterizations. By comparing coupled and uncoupled model runs, we  
398 showed that neglecting wave radiation stress gradient can induce differences  
399 of up to 1 m/s in modeled current velocities. The radiation stress gradient  
400 during the hurricane was especially large over the shelf break, where waves  
401 are strongly dissipated by the offshore coral reef barrier. The radiation stress  
402 gradient alone can deflect drifting particles by up to 5 km during the passage  
403 of the hurricane. These differences in modeled trajectories were significantly  
404 larger and required more time to stabilize on the outer shelf. The impact of  
405 the Stokes drift dominates the effects of wave-current interactions through the  
406 radiation stress gradient, except during the passage of the hurricane, when  
407 both contributions are similar. Finally, neglecting wave-current interactions  
408 when computing Stokes drift leads to variations of up to 2 km in modeled  
409 trajectories on the passage of the hurricane.

410 Despite slightly overestimating the amplitude of the sea surface elevation in  
411 fair weather conditions, the coupled wave-current model correctly reproduces  
412 the timing and amplitude of the observed storm surge. All elevation peaks are  
413 captured with a 4% accuracy at every station except Virginia key, where the  
414 surge was overestimated by about 15%. Such accuracy is key to predict the  
415 damages caused by the hurricane, as most destroyed and severely damaged  
416 buildings in the Florida Keys during Hurricane Irma were caused by storm  
417 surge and waves (Xian et al., 2018). Furthermore, by using a high-resolution  
418 model, we can explicitly reproduce the circulation between all the reefs and  
419 islands of the Florida Keys. The fine-scale details of the storm surge, and  
420 hence the associated risk, are thus accurately represented. In addition to  
421 accurately capturing positive surges, the model also reproduced the observed  
422 negative surge in Naples with an error of about 1%. This result is of interest  
423 from a biological point of view as negative surges, although less studied, affect  
424 water exchanges between the estuaries and the coastal ocean and disturb  
425 the benthic ecosystems (Liu et al., 2020). Such rapid decrease in water  
426 level followed by a positive surge cause massive freshwater inflows, causing a

427 significant decrease in water salinity (Wachnicka et al., 2019).

428 Strong currents such as the Gulf Stream affect waves through refraction  
429 over gradients in current velocity, shoaling and breaking of opposing waves or  
430 lengthening of following waves (Hegermiller et al., 2019). Under hurricane  
431 conditions, these interactions can cause numerical instabilities in the wave  
432 model if the parameterizations are not appropriate and the model resolution  
433 is not sufficient. Hegermiller et al. (2019), for instance, used a 5-km model  
434 grid and 48 directional bins to capture spatial gradients in wave height  
435 induced by wave-currents interactions in the Gulf Stream during Hurricane  
436 Matthew (2016). We followed these guidelines when defining the coarsest  
437 resolution of the model mesh as well as the spectral discretization of SWAN.  
438 Boundary conditions and directional spreading of the incident waves also  
439 play a significant role when modeling wave-current interactions at meso-  
440 and submesoscales (Villas Bôas et al., 2020), which motivated our choice  
441 of imposing full spectra on the boundary of the wave model instead of  
442 bulk parameters. Finally, SWAN default parameterizations for wind energy  
443 input and whitecapping caused numerical instabilities by overestimating wave  
444 growth and steepness on the boundary of the Gulf Stream on the passage  
445 of Irma. This overestimation was solved by using the parameterization  
446 of Siadatmousavi et al. (2011). The parameters used in this study were  
447 calibrated on the Northern Gulf of Mexico, which might explain that our  
448 model better reproduces wave parameters at buoys located on the WFS.  
449 However, these calibrated parameters might underestimate wind-induced  
450 wave growth on Florida's eastern shelf. Consequently, incident wave do not  
451 receive enough energy to grow after breaking on the bank boundary, leading to  
452 an underestimation of the significant wave height at buoys located on Florida's  
453 eastern shelf. A more extensive calibration study might therefore be necessary  
454 to further improve the agreement with field measurements on both sides of  
455 Florida. Nonetheless, as this study focuses on the wave produced by Irma,  
456 which made landfall on the West coast of Florida, the use of parameterizations

457 calibrated for the Gulf of Mexico seems reasonable.

458 The radiation stress gradient significantly impacts currents during the  
459 passage of the hurricane. It can induce differences of up to 1 m/s in the  
460 current speed on the shelf break. In this region waves are strongly dissipated  
461 due to action of depth-induced breaking and bottom dissipation on coral reefs.  
462 This highlights the protective role of coral reefs against strong incoming waves  
463 (Lowe et al., 2005), which requires a sufficiently fine spatial resolution to be  
464 explicitly represented in the model. Due to the dissipation of incoming waves  
465 on the reefs, wave impact during Irma is different on the inner and outer  
466 shelves. It is less important on the inner shelf because of the sheltering of the  
467 inner shelf due to reefs and islands as well as wave breaking on the shelf break.  
468 The inner shelf hence experiences weaker waves and currents, inducing weaker  
469 and more localized transport. Furthermore, the impact of winds on waves  
470 is reduced in shallower areas under the action of depth-induced breaking.  
471 This might explain why differences between particle trajectories stabilize  
472 on the inner shelf just after the passage of Hurricane Irma. However, the  
473 Florida Keys still experienced strong winds after the passage of the core of the  
474 hurricane, which generated high waves in the deeper areas. This might explain  
475 why the differences on between the modeled trajectories kept increasing on  
476 the outer shelf under the action of strong Stokes drift up to two days after  
477 the passage of the hurricane.

478 The distance between the centers of mass of the particle clouds advected  
479 by coupled and uncoupled Stokes drift remains rather limited (< 2 km). This  
480 suggest that taking wave-current interactions into account when computing  
481 Stokes drift, even in heavy wind conditions has a limited impact. Furthermore,  
482 combining the coupled Stokes drift with the coupled and uncoupled SLIM  
483 currents produced similar trajectories on the inner shelf, which seems to  
484 indicate that wave impact on currents is limited in this region. This would  
485 suggest that it is not necessary to take wave-current interactions into account  
486 when modeling the trajectories of tracers in shallow, sheltered areas such

487 as the inner WFS during a hurricane. Uncoupled currents with uncoupled  
488 Stokes drift should give a reasonably accurate approximation of the transport  
489 processes. However, this does not hold for deeper and unsheltered regions,  
490 as highlighted by the comparison of trajectories obtained with coupled and  
491 uncoupled SLIM currents combined with coupled Stokes drift on the outer  
492 shelf.

## 493 5. Conclusion

494 We developed a coupled wave-current model to study the impact of waves  
495 on transport processes during Hurricane Irma. In order to accurately represent  
496 the wind and pressure profiles of the hurricane, we built hybrid fields by  
497 combining coarser ERA-5 data with high-resolution H\*Wind data for the wind  
498 speed and idealized Holland profiles for the pressure. Comparing these hybrid  
499 profiles with field observations showed that they were better at reproducing the  
500 observed central depression of the hurricane as well as the peak in wind speed  
501 than ERA-5 data. Using these hybrid fields as forcings, our coupled model  
502 accurately reproduced the storm surge at tide gauge locations and produced  
503 currents and wave parameters in good agreement with field observations,  
504 especially on the WFS. The modeled currents and Stokes drift were then used  
505 to evaluate the impact of waves on the trajectory of passive drifters on the  
506 passage of the hurricane through the Florida Keys. Our results show that  
507 waves had a significant impact on heavy-wind transport processes and caused  
508 deflections of the drifters trajectories by more than 20 km on the outer shelf.

509 Despite its good agreement with observations, our model could be fur-  
510 ther refined by improving the representation of wind-wave interactions. In  
511 particular, it does not consider the momentum loss due to the action of  
512 surface waves when representing momentum flux from the atmosphere to the  
513 ocean, leading to overestimations under hurricane conditions. Our model  
514 could therefore be further improved by using wave-dissipative stress instead  
515 of the full wind stress as the momentum flux from the atmosphere to the

ocean. Moreover, a more thorough calibration of the wave model parameters should improve our model results on Florida's eastern shelf. Finally, as a 2D barotropic model, SLIM does not explicitly represent baroclinic phenomena as well as the vertical profile of the Stokes drift and radiation stress gradient along the wave boundary layer. However, our study focused on relatively shallow and vertically homogeneous coastal waters using a reef-scale resolution throughout the whole FRT. Such fine resolution allows to explicitly represent wave dissipation over coral reefs and is only achievable using a 2D model due to computational resources limitations.

Wave coupling needs to be taken into account during heavy-wind events but not necessarily in milder conditions. While the radiation stress gradient plays an important role and can lead to differences of up to 5 km, the Stokes drift is about 4 times more intense and should thus be considered in priority. This study brings new insight on the impact of waves on the transport processes nearshore during a tropical cyclone. Due to its high spatial resolution, the developed coupled wave-current model can be used to accurately represent the dispersal of pollutants, sediments or larvae in topologically complex coastal areas in heavy-wind conditions.

## Acknowledgments

Computational resources were provided by the Consortium des Équipements de Calcul Intensif (CÉCI), funded by the F.R.S.-FNRS under Grant No. 2.5020.11. Thomas Dobbelaere is a PhD student supported by the Fund for Research training in Industry and Agriculture (FRIA/FNRS).

## References

Bever, A.J., MacWilliams, M.L., 2013. Simulating sediment transport processes in San Pablo Bay using coupled hydrodynamic, wave, and sediment transport models. *Marine Geology* 345, 235–253.

- 543 Bhatia, K.T., Vecchi, G.A., Knutson, T.R., Murakami, H., Kossin, J., Dixon,  
544 K.W., Whitlock, C.E., 2019. Recent increases in tropical cyclone intensification  
545 rates. *Nature Communications* 10, 1–9.
- 546 Booij, N., Ris, R.C., Holthuijsen, L.H., 1999. A third-generation wave  
547 model for coastal regions: 1. Model description and validation. *Journal of  
548 Geophysical Research: Oceans* 104, 7649–7666.
- 549 Breivik, Ø., Allen, A.A., Maisondieu, C., Olagnon, M., 2013. Advances in  
550 search and rescue at sea. *Ocean Dynamics* 63, 83–88.
- 551 Chassignet, E.P., Hurlburt, H.E., Smedstad, O.M., Halliwell, G.R., Hogan,  
552 P.J., Wallcraft, A.J., Baraille, R., Bleck, R., 2007. The HYCOM (hybrid  
553 coordinate ocean model) data assimilative system. *Journal of Marine  
554 Systems* 65, 60–83.
- 555 Craik, A.D., Leibovich, S., 1976. A rational model for Langmuir circulations.  
556 *Journal of Fluid Mechanics* 73, 401–426.
- 557 Curcic, M., 2015. Explicit air-sea momentum exchange in coupled atmosphere-  
558 wave-ocean modeling of tropical cyclones. Ph.D. thesis. University of Miami.
- 559 Curcic, M., Chen, S.S., Özgökmen, T.M., 2016. Hurricane-induced ocean  
560 waves and stokes drift and their impacts on surface transport and dispersion  
561 in the Gulf of Mexico. *Geophysical Research Letters* 43, 2773–2781.
- 562 Curcic, M., Haus, B.K., 2020. Revised estimates of ocean surface drag in  
563 strong winds. *Geophysical Research Letters* 47, e2020GL087647.
- 564 Dietrich, J., Bunya, S., Westerink, J., Ebersole, B., Smith, J., Atkinson,  
565 J., Jensen, R., Resio, D., Luettich, R., Dawson, C., et al., 2010. A high-  
566 resolution coupled riverine flow, tide, wind, wind wave, and storm surge  
567 model for southern Louisiana and Mississippi. Part II: Synoptic description  
568 and analysis of Hurricanes Katrina and Rita. *Monthly Weather Review*  
569 138, 378–404.

- 570 Dietrich, J., Westerink, J., Kennedy, A., Smith, J., Jensen, R., Zijlema, M.,  
571 Holthuijsen, L., Dawson, C., Luettich, R., Powell, M., et al., 2011. Hurricane  
572 Gustav (2008) waves and storm surge: Hindcast, synoptic analysis, and  
573 validation in southern Louisiana. *Monthly Weather Review* 139, 2488–2522.
- 574 Dietrich, J.C., Tanaka, S., Westerink, J.J., Dawson, C., Luettich, R., Zijlema,  
575 M., Holthuijsen, L.H., Smith, J., Westerink, L., Westerink, H., 2012. Per-  
576 formance of the unstructured-mesh, SWAN+ ADCIRC model in computing  
577 hurricane waves and surge. *Journal of Scientific Computing* 52, 468–497.
- 578 Dobbelaere, T., Muller, E.M., Gramer, L.J., Holstein, D.M., Hanert, E., 2020.  
579 Coupled epidemic-hydrodynamic modeling to understand the spread of a  
580 deadly coral disease in Florida. *Frontiers in Marine Science* 7, 1016.
- 581 Donelan, M., Haus, B., Reul, N., Plant, W., Stiassnie, M., Graber, H., Brown,  
582 O., Saltzman, E., 2004. On the limiting aerodynamic roughness of the  
583 ocean in very strong winds. *Geophysical Research Letters* 31.
- 584 Drivdal, M., Broström, G., Christensen, K., 2014. Wave-induced mixing and  
585 transport of buoyant particles: Application to the Statfjord A oil spill.  
586 *Ocean Science* 10, 977–991.
- 587 Figueiredo, J., Baird, A.H., Connolly, S.R., 2013. Synthesizing larval com-  
588 petence dynamics and reef-scale retention reveals a high potential for  
589 self-recruitment in corals. *Ecology* 94, 650–659.
- 590 Fringer, O.B., Dawson, C.N., He, R., Ralston, D.K., Zhang, Y.J., 2019. The  
591 future of coastal and estuarine modeling: Findings from a workshop. *Ocean  
592 Modelling* 143, 101458.
- 593 Frys, C., Saint-Amand, A., Le Hénaff, M., Figueiredo, J., Kuba, A., Walker,  
594 B., Lambrechts, J., Vallaey, V., Vincent, D., Hanert, E., 2020. Fine-scale  
595 coral connectivity pathways in the Florida Reef Tract: Implications for  
596 conservation and restoration. *Frontiers in Marine Science* 7, 312.

- 597 Geuzaine, C., Remacle, J.F., 2009. Gmsh: A 3-d finite element mesh generator  
598 with built-in pre-and post-processing facilities. International journal for  
599 numerical methods in engineering 79, 1309–1331.
- 600 Harper, B., Kepert, J., Ginger, J., 2010. Guidelines for converting between  
601 various wind averaging periods in tropical cyclone conditions.
- 602 Hegermiller, C.A., Warner, J.C., Olabarrieta, M., Sherwood, C.R., 2019.  
603 Wave-current interaction between Hurricane Matthew wave fields and the  
604 Gulf Stream. Journal of Physical Oceanography 49, 2883–2900.
- 605 Hoefel, F., Elgar, S., 2003. Wave-induced sediment transport and sandbar  
606 migration. Science 299, 1885–1887.
- 607 Holthuijsen, L.H., Powell, M.D., Pietrzak, J.D., 2012. Wind and waves in  
608 extreme hurricanes. Journal of Geophysical Research: Oceans 117.
- 609 Janssen, P.A., 1991. Quasi-linear theory of wind-wave generation applied to  
610 wave forecasting. Journal of Physical Oceanography 21, 1631–1642.
- 611 Johns, W.E., Schott, F., 1987. Meandering and transport variations of the  
612 Florida Current. Journal of Physical Oceanography 17, 1128–1147.
- 613 Knaff, J.A., Sampson, C.R., Musgrave, K.D., 2018. Statistical tropical cyclone  
614 wind radii prediction using climatology and persistence: Updates for the  
615 western North Pacific. Weather and Forecasting 33, 1093–1098.
- 616 Knutson, T., Camargo, S.J., Chan, J.C., Emanuel, K., Ho, C.H., Kossin, J.,  
617 Mohapatra, M., Satoh, M., Sugi, M., Walsh, K., et al., 2020. Tropical  
618 cyclones and climate change assessment: Part II: Projected response to  
619 anthropogenic warming. Bulletin of the American Meteorological Society  
620 101, E303–E322.

- 621 Komen, G., Hasselmann, S., Hasselmann, K., 1984. On the existence of a  
622 fully developed wind-sea spectrum. *Journal of Physical Oceanography* 14,  
623 1271–1285.
- 624 Kossin, J.P., Knapp, K.R., Olander, T.L., Velden, C.S., 2020. Global increase  
625 in major tropical cyclone exceedance probability over the past four decades.  
626 *Proceedings of the National Academy of Sciences* 117, 11975–11980.
- 627 Kourafalou, V.H., Kang, H., 2012. Florida Current meandering and evo-  
628 lution of cyclonic eddies along the Florida Keys Reef Tract: Are they  
629 interconnected? *Journal of Geophysical Research: Oceans* 117.
- 630 Kundu, P.K., 1976. Ekman veering observed near the ocean bottom. *Journal*  
631 *of Physical Oceanography* 6, 238–242.
- 632 Lambrechts, J., Hanert, E., Deleersnijder, E., Bernard, P.E., Legat, V.,  
633 Remacle, J.F., Wolanski, E., 2008. A multi-scale model of the hydrodynam-  
634 ics of the whole Great Barrier Reef. *Estuarine, Coastal and Shelf Science*  
635 79, 143–151.
- 636 Landsea, C.W., Franklin, J.L., 2013. Atlantic hurricane database uncertainty  
637 and presentation of a new database format. *Monthly Weather Review* 141,  
638 3576–3592.
- 639 Lane, E.M., Restrepo, J., McWilliams, J.C., 2007. Wave-current interaction:  
640 A comparison of radiation-stress and vortex-force representations. *Journal*  
641 *of Physical Oceanography* 37, 1122–1141.
- 642 Langmuir, I., 1938. Surface motion of water induced by wind. *Science* 87,  
643 119–123.
- 644 Le, H.A., Lambrechts, J., Ortaleb, S., Gratiot, N., Deleersnijder, E., Soares-  
645 Frazão, S., 2020. An implicit wetting–drying algorithm for the discontinuous  
646 galerkin method: application to the tonle sap, mekong river basin. *Envi-  
647 ronmental Fluid Mechanics* , 1–29.

- 648 Le Hénaff, M., Kourafalou, V.H., Paris, C.B., Helgers, J., Aman, Z.M., Hogan,  
649 P.J., Srinivasan, A., 2012. Surface evolution of the Deepwater Horizon  
650 oil spill patch: Combined effects of circulation and wind-induced drift.  
651 Environmental Science & Technology 46, 7267–7273.
- 652 Lee, T.N., Leaman, K., Williams, E., Berger, T., Atkinson, L., 1995. Florida  
653 Current meanders and gyre formation in the southern Straits of Florida.  
654 Journal of Geophysical Research: Oceans 100, 8607–8620.
- 655 Lee, T.N., Mayer, D.A., 1977. Low-frequency current variability and spin-off  
656 eddies along the shelf off southeast Florida. Collected Reprints 1, 344.
- 657 Lee, T.N., Smith, N., 2002. Volume transport variability through the Florida  
658 Keys tidal channels. Continental Shelf Research 22, 1361–1377.
- 659 Lee, T.N., Williams, E., 1988. Wind-forced transport fluctuations of the  
660 Florida Current. Journal of Physical Oceanography 18, 937–946.
- 661 Li, Z., Johns, B., 1998. A three-dimensional numerical model of surface  
662 waves in the surf zone and longshore current generation over a plane beach.  
663 Estuarine, Coastal and Shelf Science 47, 395–413.
- 664 Lin, N., Chavas, D., 2012. On hurricane parametric wind and applications in  
665 storm surge modeling. Journal of Geophysical Research: Atmospheres 117.
- 666 Liu, Y., Weisberg, R.H., 2012. Seasonal variability on the West Florida shelf.  
667 Progress in Oceanography 104, 80–98.
- 668 Liu, Y., Weisberg, R.H., Zheng, L., 2020. Impacts of hurricane Irma on the  
669 circulation and transport in Florida Bay and the Charlotte Harbor estuary.  
670 Estuaries and Coasts 43, 1194–1216.
- 671 Liubartseva, S., Coppini, G., Lecci, R., Clementi, E., 2018. Tracking plastics  
672 in the Mediterranean: 2D Lagrangian model. Marine Pollution Bulletin  
673 129, 151–162.

- 674 Longuet-Higgins, M.S., 1970. Longshore currents generated by obliquely  
675 incident sea waves. *Journal of Geophysical Research* 75, 6778–6789.
- 676 Longuet-Higgins, M.S., Stewart, R., 1964. Radiation stresses in water waves;  
677 a physical discussion, with applications, in: *Deep Sea Research and Oceanographic Abstracts*, Elsevier. pp. 529–562.
- 679 Lowe, R.J., Falter, J.L., Bandet, M.D., Pawlak, G., Atkinson, M.J., Moni-  
680 smith, S.G., Koseff, J.R., 2005. Spectral wave dissipation over a barrier  
681 reef. *Journal of Geophysical Research: Oceans* 110.
- 682 Madsen, O.S., Poon, Y.K., Gruber, H.C., 1989. Spectral wave attenuation by  
683 bottom friction: Theory, in: *Coastal Engineering 1988*, pp. 492–504.
- 684 Malmstadt, J., Scheitlin, K., Elsner, J., 2009. Florida hurricanes and damage  
685 costs. *Southeastern Geographer* 49, 108–131.
- 686 McWilliams, J.C., Restrepo, J.M., Lane, E.M., 2004. An asymptotic theory  
687 for the interaction of waves and currents in coastal waters. *Journal of Fluid  
688 Mechanics* 511, 135.
- 689 McWilliams, J.C., Sullivan, P.P., 2000. Vertical mixing by Langmuir circula-  
690 tions. *Spill Science & Technology Bulletin* 6, 225–237.
- 691 Mei, C.C., 1989. The applied dynamics of ocean surface waves. volume 1.  
692 World scientific.
- 693 Moon, I.J., Ginis, I., Hara, T., Thomas, B., 2007. A physics-based parame-  
694 terization of air-sea momentum flux at high wind speeds and its impact on  
695 hurricane intensity predictions. *Monthly Weather Review* 135, 2869–2878.
- 696 Pinelli, J.P., Roueche, D., Kijewski-Correa, T., Plaz, F., Prevatt, D., Zisis,  
697 I., Elawady, A., Haan, F., Pei, S., Gurley, K., et al., 2018. Overview of  
698 damage observed in regional construction during the passage of Hurricane  
699 Irma over the State of Florida, in: *Forensic Engineering 2018: Forging*

- 700      Forensic Frontiers. American Society of Civil Engineers Reston, VA, pp.  
701      1028–1038.
- 702      Powell, M.D., Houston, S.H., Amat, L.R., Morisseau-Leroy, N., 1998. The  
703      HRD real-time hurricane wind analysis system. *Journal of Wind Engineering*  
704      and Industrial Aerodynamics
- 705      77, 53–64.
- 706      Powell, M.D., Vickery, P.J., Reinhold, T.A., 2003. Reduced drag coefficient  
707      for high wind speeds in tropical cyclones. *Nature* 422, 279–283.
- 708      Röhrs, J., Christensen, K.H., Hole, L.R., Broström, G., Drivdal, M., Sundby,  
709      S., 2012. Observation-based evaluation of surface wave effects on currents  
710      and trajectory forecasts. *Ocean Dynamics* 62, 1519–1533.
- 711      Schott, F.A., Lee, T.N., Zantopp, R., 1988. Variability of structure and  
712      transport of the Florida Current in the period range of days to seasonal.  
713      *Journal of Physical Oceanography* 18, 1209–1230.
- 714      Siadatmousavi, S.M., Jose, F., Stone, G., 2011. Evaluation of two WAM  
715      white capping parameterizations using parallel unstructured SWAN with  
716      application to the Northern Gulf of Mexico, USA. *Applied Ocean Research*  
717      33, 23–30.
- 718      Sikirić, M.D., Roland, A., Janečković, I., Tomazić, I., Kuzmić, M., 2013.  
719      Coupling of the Regional Ocean Modeling System (ROMS) and Wind  
720      Wave Model. *Ocean Modelling* 72, 59–73.
- 721      Smith, N.P., 1982. Response of Florida Atlantic shelf waters to hurricane  
722      David. *Journal of Geophysical Research: Oceans* 87, 2007–2016.
- 723      Spivakovskaya, D., Heemink, A., Milstein, G., Schoenmakers, J., 2005. Sim-  
724      ulation of the transport of particles in coastal waters using forward and  
725      reverse time diffusion. *Advances in water resources* 28, 927–938.

- 725 Stokes, G.G., 1880. On the theory of oscillatory waves. *Transactions of the*  
726 *Cambridge Philosophical Society* .
- 727 Tolman, H.L., et al., 2009. User manual and system documentation of  
728 WAVEWATCH III TM version 3.14. Technical note, MMAB Contribution  
729 276, 220.
- 730 Van Den Bremer, T., Breivik, Ø., 2018. Stokes drift. *Philosophical Trans-*  
731 *actions of the Royal Society A: Mathematical, Physical and Engineering*  
732 *Sciences* 376, 20170104.
- 733 Villas Bôas, A.B., Cornuelle, B.D., Mazloff, M.R., Gille, S.T., Arduin, F.,  
734 2020. Wave–current interactions at meso-and submesoscales: Insights from  
735 idealized numerical simulations. *Journal of Physical Oceanography* 50,  
736 3483–3500.
- 737 Wachnicka, A., Browder, J., Jackson, T., Louda, W., Kelble, C., Abdelrahman,  
738 O., Stabenau, E., Avila, C., 2019. Hurricane Irmas impact on water quality  
739 and phytoplankton communities in Biscayne Bay (Florida, USA). *Estuaries*  
740 and Coasts , 1–18.
- 741 WAMDI Group, 1988. The WAM model – A third generation ocean wave  
742 prediction model. *Journal of Physical Oceanography* 18, 1775–1810.
- 743 Weisberg, R., Liu, Y., Mayer, D., 2009. Mean circulation on the west Florida  
744 continental shelf observed with long-term moorings. *Geophys. Res. Lett*  
745 36, L19610.
- 746 Weisberg, R.H., Zheng, L., 2006. Hurricane storm surge simulations for  
747 Tampa Bay. *Estuaries and Coasts* 29, 899–913.
- 748 Wu, L., Chen, C., Guo, P., Shi, M., Qi, J., Ge, J., 2011. A FVCOM-  
749 based unstructured grid wave, current, sediment transport model, I. Model  
750 description and validation. *Journal of Ocean University of China* 10, 1–8.

- 751 Xian, S., Feng, K., Lin, N., Marsooli, R., Chavas, D., Chen, J., Hatzikyriakou,  
752 A., 2018. Brief communication: Rapid assessment of damaged residential  
753 buildings in the Florida Keys after Hurricane Irma. *Natural Hazards and*  
754 *Earth System Sciences* 18, 2041–2045.
- 755 Zedler, S., Niiler, P., Stammer, D., Terrill, E., Morzel, J., 2009. Ocean's  
756 response to Hurricane Frances and its implications for drag coefficient  
757 parameterization at high wind speeds. *Journal of Geophysical Research: Oceans* 114.
- 759 Zhang, C., Durgan, S.D., Lagomasino, D., 2019. Modeling risk of mangroves  
760 to tropical cyclones: A case study of Hurricane Irma. *Estuarine, Coastal and Shelf Science* 224, 108–116.  
761